Control of the Magnon-Photon Level Attraction in a Planar Cavity

Y. Yang,[1,2] J.W. Rao,[1,*] Y.S. Gui,[1] B.M. Yao,[2] W. Lu,[2] and C.-M. Hu[1,†]

[1]*Department of Physics and Astronomy, University of Manitoba, Winnipeg R3T 2N2, Canada*

[2]*State Key Laboratory of Infrared Physics, Chinese Academy of Science, 200083 Shanghai, China*

A resistive coupling circuit is used to model the recently discovered dissipative coupling in a hybridized cavity photon-magnon system. With this model as a basis we design a planar cavity in which a controllable transition between level attraction and level repulsion can be achieved. This behavior can be quantitatively understood using an *LCR*-circuit model with a complex coupling strength. Our work therefore develops and verifies a circuit method to model level repulsion and level attraction and confirms the universality of dissipative coupling in the cavity photon-magnon system. The realization of both coherent coupling and dissipative coupling in a planar cavity may provide new avenues for the design and adaptation of dissipatively coupled systems for practical applications in information processing.

I. INTRODUCTION

Strong light-matter interactions are an interesting and important subject in condensed matter physics, enabling new insight into material characteristics and device design [1–7]. Of key importance is the phenomena of Rabi splitting—the removal of an energy degeneracy due to hybridization, which offers new possibilities for coherent manipulation. Numerically, the vacuum Rabi splitting is twice the product of the transition dipole moment and the vacuum field arising from the root-mean-square of the vacuum fluctuations [8]. To date, coherent interaction between confined electromagnetic fields and a qubit [9–11], a quantum dot [12], a mechanical oscillator [13,14], and a magnon [15–17] has been demonstrated. In particular, due to the low room-temperature damping rate of microwave photons and magnons and the maturation of microwave technology, the cavity photon-magnon system [18] has been brought to the forefront, providing an interesting platform for the merging of quantum electrodynamics and magnetism. Recent progress has demonstrated ultrastrong coupling [19–21], gradient memory architectures [22], the control and read-out of qubit states [23], spin-pumping manipulation [18,24], and cooperative polariton dynamics [25].

At microwave frequencies, such hybrid circuits involving charges, spins, and solid-state devices can be fabricated on a chip and integrated with well-established microwave technologies, which are crucial for the future development of information processing [3]. The engineering ability of

coherent coupling has been made feasible by the development of phenomenologically equivalent *LCR* models for such circuits. Depending on the dominant electric or magnetic nature of the confined electromagnetic field, strong light-matter interactions have been modeled by the introduction of mutual capacitance for a phase qubit [10,26], a quantum dot [27], and an optomechanical device [28] or mutual inductance for a flux qubit [29,30] and a cavity photon-magnon system [31]. This approach successfully reproduces the key physical phenomena associated with coherently coupled systems, while also enabling on-chip integration.

However, the coupling between light and matter is not strictly limited to coherent interactions. Very recently, dissipative-coupling-induced level attraction was experimentally discovered, where hybridized modes coalesce rather than repel, due to a Lenz-like effect in a Fabry-Perot cavity [32]. Such behavior cannot be described by mutual capacitive or inductive mechanisms. Therefore, device integration requires a more-general equivalent *LCR* model. While the physical meaning is very different, from a mathematical point of view, level attraction and level repulsion are equivalent to each other through frequency and damping exchange in the plane of complex eigenvalues [33–35]. For level repulsion, the eigenfrequencies, corresponding to the real eigenspectrum, are repelled, while the damping parameters of the hybridized modes, determined by the imaginary eigenspectrum, are attracted. The opposite is true for level attraction. This relationship hints at a more comprehensive *LCR*-circuit model that includes both repulsion and attraction—the imaginary coupling strength required for level attraction should be produced by a mutual resistance that accounts for the dissipative

---
*jinweir@myumanitoba.ca
†hu@physics.umanitoba.ca

coupling, while the real coupling strength, which leads to level repulsion, will arise from a mutual capacitance or inductance [36,37].

Typically, the mutual resistive coupling is concealed behind the dominant capacitive and inductive mechanisms. However, in the work reported here we couple $Y_3Fe_5O_{12}$ (YIG) to a specially designed planar microstrip cross junction that enables both level attraction and level repulsion. By tuning the YIG position, we can manipulate the local-rf-field distribution and transition between level repulsion, with inductance-dominated coupling, and level attraction, with resistance-dominated coupling. Level attraction in such an on-chip device may provide new avenues for the integrability and practical design of information processing.

II. EXPERIMENT

A picture of the microstrip-cross-junction cavity is depicted in Fig. 1(a). Details of the design and characterization of this cavity are given in the Appendix. During our experiment the x-y plane of this cavity is fixed inside an electromagnet, which provides an external magnetic field H along the z direction. To observe photon-magnon coupling, a 1-mm-diameter YIG sphere, chosen for its high spin density, low losses, and therefore large photon-magnon coupling [38], is mounted on an x-y-z stage at a fixed height $D = 0.7$ mm from the cavity in the z direction. This setup allows us to continuously tune the YIG position in the x-y plane, and hence to change the local field and the coupling effect. In our experiment the YIG sphere (black circle) can be moved within the 10×10 mm^2 range of the dashed blue box shown in Fig. 1(a). The cavity transmission spectrum S_{21} (green symbols) is displayed in Fig. 1(c), where three resonant modes, with frequencies of $\omega_c/2\pi =$ 3.22, 6.253, and 9.39 GHz, are labeled as "mode 1," "mode 2," and "mode 3." A detailed discussion of the cavity resonance can be found in the Appendix. Black and red curves correspond to theoretical calculations performed with Eq. (A2b) and Computer Simulation Technology Microwave Studio (CST MWS) simulations, respectively.

Essentially, the coupling mechanism of coupling effects in the coupled cavity photon-magnon system can be defined by three fundamental electrodynamic principles: Ampère's law, Faraday's law, and Lenz's law [32]. Specifically, the inductive current of the cavity induces a magnetic field (Ampère's law), which applies a driving torque to the spin in the magnon system (the YIG sphere). Because of the spin precession, the magnetic flux of the cavity is altered. As a consequence, an induced current is generated in the cavity circuit (Faraday's law), which affects the dynamic properties of the cavity mode. Usually these two principles dominate, leading to a coherent coupling in the cavity photon-magnon system. However, in some special cases, such as in the cross cavity, another electrodynamic
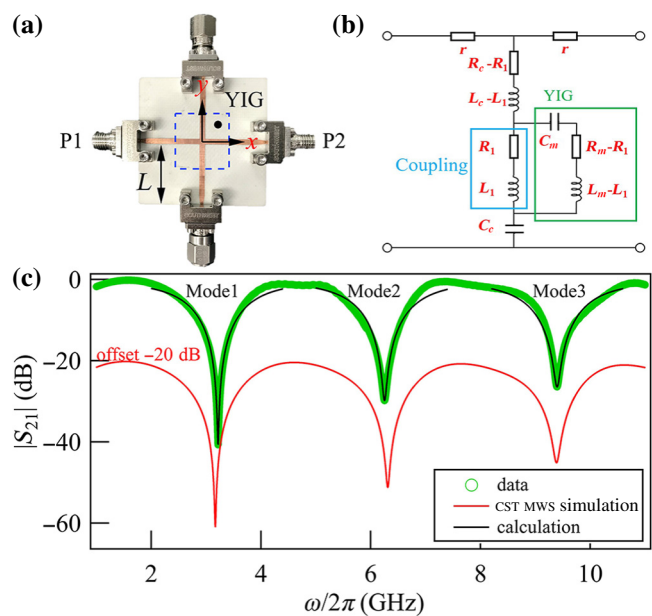

FIG. 1. (a) The measurement setup with a 1-mm-diameter YIG sphere placed D = 0.7 mm above the planar microstrip-cross-junction cavity. The two short-terminated vertical arms and the two horizontal arms all have length L = 20 mm. The planar cavity is placed in the x-y plane, while an external magnetic field H is applied in the z direction (perpendicular to the planar cavity). The range of YIG locations is indicated by the 10×10 mm^2 dashed blue box. (b) Equivalent circuit of the coupled system. Circuit elements used to model the YIG sphere are highlighted by the green box, while the coupling term is emphasized by a blue box. (c) Cavity spectra of experimental data (green), theory (black), and CST MWS simulation (red, -20 dB offset), with three resonant modes labeled "mode 1," "mode 2," and "mode 3."

principle, Lenz's law, must also be considered. In such cases an additional magnetic field is generated by the induced current of the spin procession, which applies a drag torque and tends to impede the spin procession (Lenz's law). Therefore, we conclude that the coupling is coherent if the driving torque due to Ampère's law is dominant over the drag torque from Lenz's law. Otherwise, the coupling effect becomes dissipative.

To demonstrate the significance of these principles for concrete applications, in this paper we propose a phenomenological *LCR* model for both coherent coupling and dissipative coupling in different physical systems. The equivalent *LCR* circuit, specific to the coupled cavity photon-magnon system reported in this paper, is shown in Fig. 1(b). To couple with the cavity circuit, the YIG sphere acts as a resonant circuit, with self-inductance, self-capacitance, and self-resistance connected in series and labeled as L_m, C_m, and R_m, respectively. To describe the coupling we consider both direct and indirect interactions between the cavity electromagnetic fields and the magnetic material. First, the electromagnetic field will be directly influenced by the permittivity and permeability,

which in general can be modeled by a mutual capacitance and inductance, respectively [31,37,39,40]. Because of the magnetic properties of YIG, we can describe the coherent coupling effects due to the resonant permeability through a mutual inductance. In other words, the rf cavity current will produce a magnetic field, which drives magnetization precession and induces a voltage in the cavity circuit. This coupling between the cavity current and the YIG is characterized by the mutual inductance, which is the ratio between the induced YIG voltage and the time derivative of the varying cavity current [41,42]. However, there is also an indirect interaction whereby the induced electric field of the YIG sphere will produce an additional cavity current due to the finite cavity conductivity. This coupling is related to damping and energy dissipation. It may be modeled by a mutual resistance [37,43], and could be realized by the 90° phase lag in the coupling term when compared with the coherent coupling. Therefore, we choose a combination of mutual inductance L_1 and mutual resistance R_1 to describe both the magnetic inductive coupling of level repulsion and the resistive

coupling of level attraction [36]. The equivalent circuit of the coupled system is shown in Fig. 1(b).

With use of the *LCR*-circuit model, the transmission spectra of the magnon-photon coupled system can be calculated as

$$S_{21} \propto 1 - \frac{i\gamma_{ce}}{\omega - \omega_c + i(\gamma_{ce} + \gamma_{ci}) + \frac{G^2}{\omega - \omega_m + i\gamma_m}}, \quad (1)$$

where $\omega_c = 1/\sqrt{L_c C_c}$ and $\omega_m = 1/\sqrt{L_m C_m}$ are the resonance frequencies of the cavity and the magnon, respectively, $\gamma_m = R_m/2L_m$ is the YIG damping, and γ_{ce} and γ_{ci} are the extrinsic and intrinsic cavity damping (see the Appendix for detailed discussion of cavity transmission). The complex coupling strength $G = (L_1\omega + iR_1)/\sqrt{4L_c L_m}$ is related to the mutual inductance and resistance. For level repulsion, L_1 is dominant, the coupling strength is real, and the hybridized modes are repelled. For level attraction, L_1 diminishes and results in an imaginary coupling strength due to R_1. In this case the modes are attracted by the coupling. To be consistent with the notation in Ref. [32], we
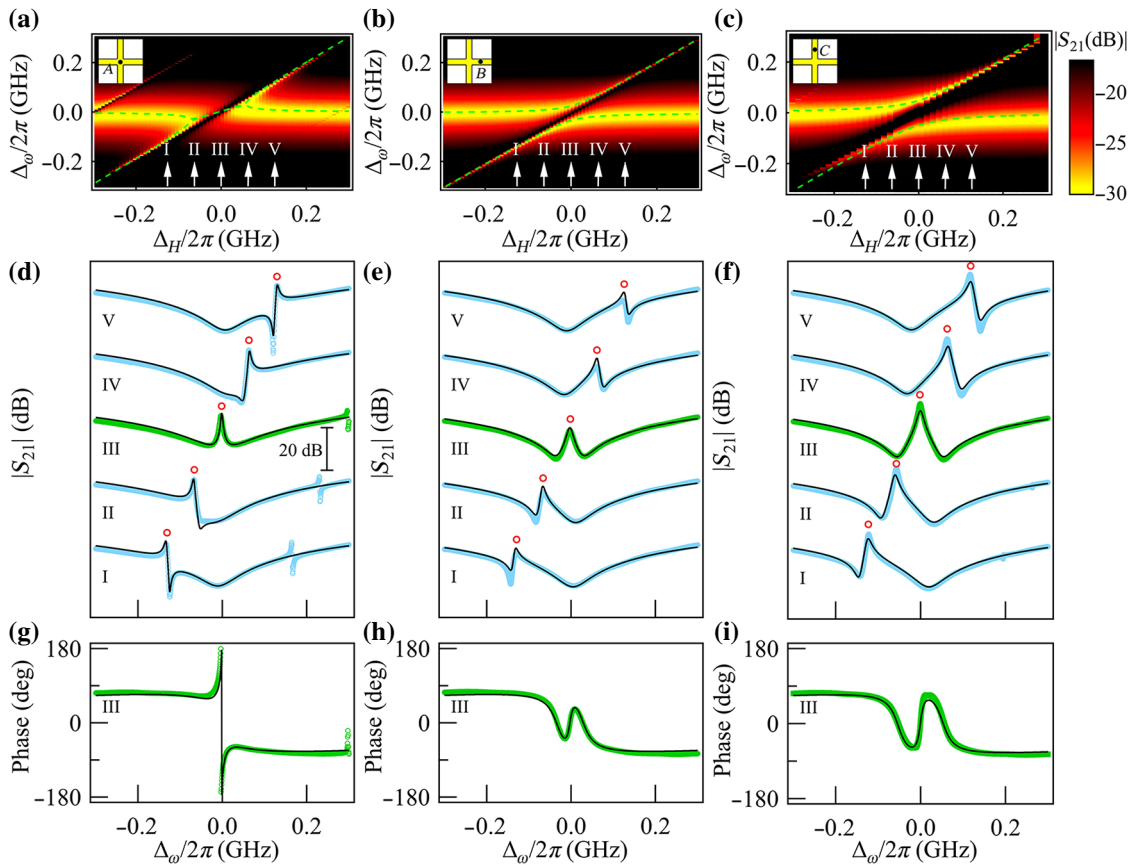

FIG. 2. (a) S_{21} amplitude mapping, (d) S_{21} amplitude spectra, and (g) S_{21} phase spectra of level attraction when YIG is mounted at position A. (b) S_{21} amplitude mapping, (e) S_{21} amplitude spectra, and (h) S_{21} phase spectra of level attraction when YIG is mounted at position B. (c) S_{21} amplitude mapping, (f) S_{21} amplitude spectra, and (i) S_{21} phase spectra of level attraction when YIG is mounted at position C. Amplitude peaks are labeled as red circles in the amplitude spectra. The dashed green lines in the amplitude mappings and the black curves in the amplitude and phase spectra are theoretical calculations.

choose an absolute value of the coupling strength $|G| = |ge^{i\Phi/2}|$. Therefore, for pure level repulsion, $\Phi = 0$ and the absolute coupling strength is $|g| = L_1\omega/\sqrt{4L_cL_m}$, while for pure level attraction, $\Phi = \pi$ and $|g| = R_1/\sqrt{4L_cL_m}$. Experimentally, during level repulsion, two hybridized modes of the system repel each other in the frequency domain when the coherent coupling is dominant. By contrast, during level attraction, the two hybridized modes coalesce with each other and occur when dissipative coupling becomes dominant.

An amplitude mapping of the microwave transmission spectra S_{21}, measured with a vector network analyzer with the YIG in the center of the cross junction at position A, is shown in Fig. 2(a) as a function of the frequency and field detunings, $\Delta_\omega = \omega - \omega_c$ and $\Delta_H = \omega_r(H) - \omega_c$. Here we use mode 2 with $\omega_c/2\pi = 6.253$ GHz. The uncoupled magnon mode with damping $\gamma_m/2\pi = 0.004$ GHz follows the Kittel dispersion $\omega_r(H) = \gamma(H + H_A)$, where $\gamma = 2\pi \times 27.4 \mu_0$ GHz/T is the gyromagnetic ratio and $\mu_0 H_A = 2.26$ mT is the magnetocrystalline anisotropy field.

At position A, a high symmetric point of the structure, where both the rf electric field and magnetic field are a minimum no matter which port is the input [see Figs. 6(c) and 6(f)], we observe level attraction by tuning the ferromagnetic resonance frequency around ω_c. The hybridized frequencies bend toward each other and meet at two exceptional points [32,33]. In the region between these two points, the modes coalesce and the absolute coupling strength is $|g/2\pi| = 33$ MHz. To change the coupling feature, we move the YIG in the x-y plane to positions B and C. The field distribution at position B is shown in Figs. 6(c) and 6(f). Although no field is input at port 2 while S_{21} is measured, the vacuum field couples to the magnons and leads to magnon-photon Rabi oscillations [44]. As shown in Figs. 2(b) and 2(c), level repulsion is observed at position B ($x = 1.82$ mm) in the right arm and at position C ($y = 1.82$ mm) in the upper arm. In these cases the two hybridized modes are repelled by each other and open a Rabi-like gap, with a coupling strength of 32.5 and 54 MHz respectively, determined by the splitting.

In Fig. 2(d) when the field detuning is set to $\Delta_H = 0$, the transmission-spectrum amplitude of level attraction is plotted as a function of Δ_ω as green circles. A resonance peak appears at $\Delta_\omega = 0$. However, it looks quite similar to the zero-detuning spectrum of level repulsion in Figs. 2(e) and 2(f). Fortunately the amplitude peaks in our system, characterized by a suppression of the $|S_{21}|$ amplitude originating from the destructive interference between the magnon response and driving force [45], can be used to distinguish the two forms of coupling. For the known case of level repulsion, shown in Figs. 2(e) and 2(f), the amplitude peak always appears between the coupled modes. However, in the case of level attraction, the peak appears outside the two hybridized modes.

Another robust method to distinguish level attraction and level repulsion is to examine the transmission phase at $\Delta_H = 0$. In level attraction, a single 2π-phase jump at $\Delta_\omega = 0$ is observed in Fig. 2(g), corresponding to an amplitude peak between the two attracted modes. In level repulsion, the amplitude dip at each hybridized mode corresponds to two π-phase delays, while the peak in between is observed as an opposite π-phase shift at $\Delta_\omega = 0$ [45,46]; see Figs. 2(h) and 2(i). Both techniques are in agreement and confirm the presence of level attraction in the transmission spectra of Fig. 2(d).

To examine the transition between level attraction and level repulsion we move the YIG position continuously along the x axis, in the range $|x| < 5$ mm. Selected YIG positions and the corresponding mappings are shown in Fig. 3, demonstrating the systematic evolution between
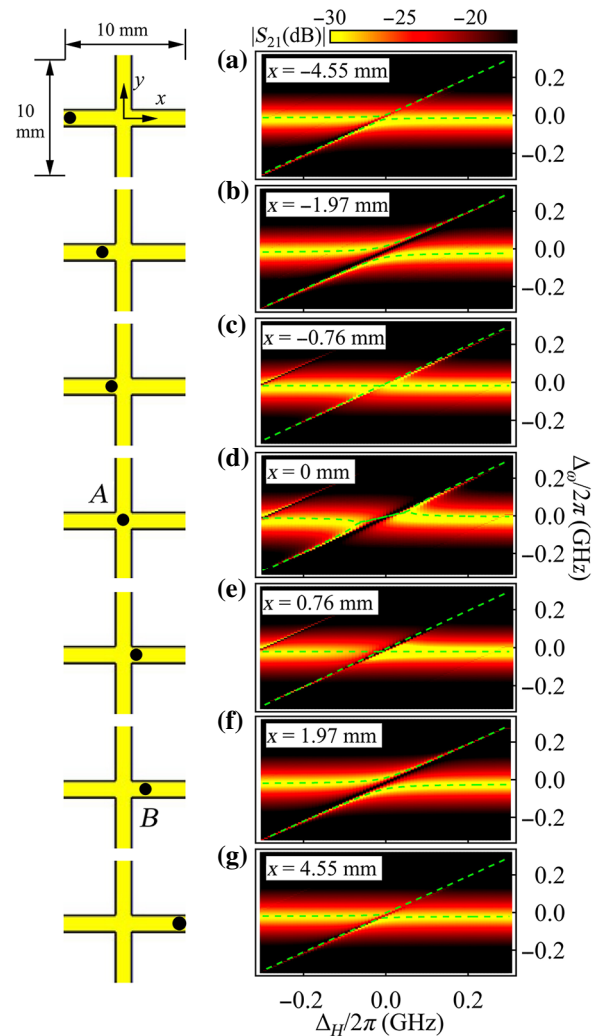

FIG. 3. In the left panel, the positions of YIG are given within a 10×10 mm^2 area. Amplitude mappings in the right panel show a systematic evolution from level repulsion to level attraction and back to level repulsion. The dashed green lines in the amplitude mappings are theoretical calculations.
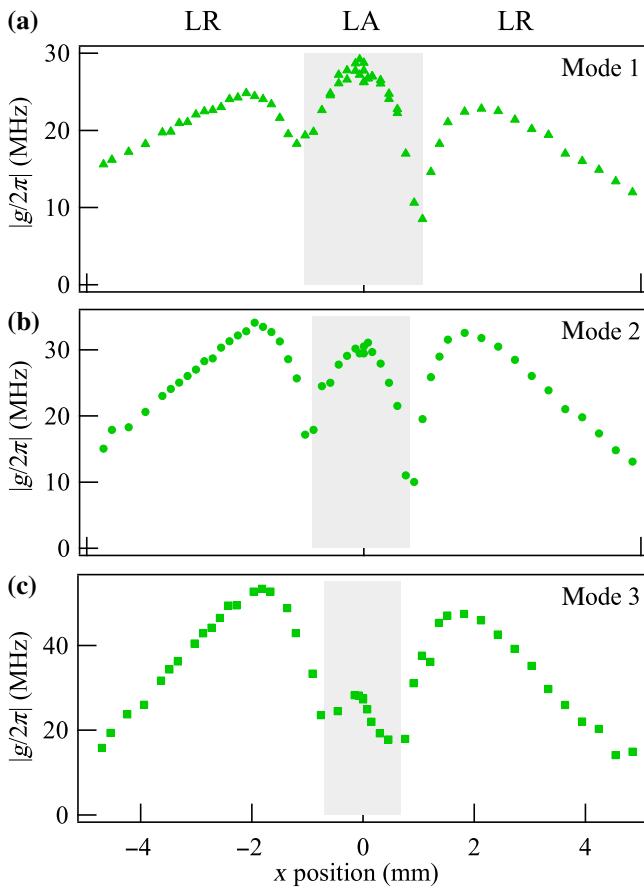
FIG. 4.   Evolution of the absolute coupling strength, $|g|$, for (a) mode 1, (b) mode 2, and (c) mode 3 when YIG is moved from $x = -5$ mm to $x = 5$ mm with $y = 0$ mm. The shaded region indicates level attraction (LA). LR, level repulsion.

level repulsion and level attraction about the crossing point $(x = 0$ mm, $y = 0$ mm). When the $|x|$ position is changed from $|x| = 4.55$ mm to $|x| = 0.76$ mm, the inductive coupling is dominant and the mapping shows level repulsion. The Rabi-like gap between the two hybridized modes increases at first, reaching a maximum at $|x| = 1.97$ mm, after which the gap gradually closes, reaching a minimum at $|x| = 0.76$ mm, where the two modes appear to cross. After $|x| = 0.76$ mm the system enters a level-attraction region, dominated by resistive coupling, and the coupling strength again increases. At $x = 0$ mm the strongest level attraction is observed.

The dependence of the coupling strength on the YIG sphere's x position can be determined for all three modes by use of Eq. (1) to fit S_{21}. The results are summarized in Fig. 4. In the shaded region the system is dominated by resistive coupling, where level attraction is observed. This is in contrast to the region of level repulsion dominated by inductive coupling. At $|x| = 5$ mm a small inductance leads to weak level repulsion. As $|x|$ decreases, the Rabi-like gap gradually opens and the coupling strength

increases to its maximum value, meaning that the inductance must increase and the interaction proceeds via the magnetic field. The mutual inductance then begins to decrease, and then the mutual resistance R_1 emerges and grows in the near-level-crossing condition. When the overall coupling strength reaches a minimum, a level crossing appears and marks the transition. As $|x|$ is decreased further beyond the crossing condition toward zero, level attraction is observed, with maximum effect at $|x| = 0$ due to the indirect interaction between the photon and magnon modes. Consistent with a previous study using a special Fabry-Perot-like resonator [32], it is clearly seen that two competing magnon-photon coupling effects coexist in the general experimental conditions in our planar cavity.

III. CONCLUSIONS

In this work we develop an *LCR*-circuit model to describe both level repulsion and its transition into level attraction, and experimentally demonstrate the existence of mutual-resistive-coupling-induced level attraction in a planar cavity. The realization of resistive coupling provides a new avenue for the development of circuit designs that implement the phenomenon of level attraction. By realization of such an on-chip device, future coupling modules may be more-easily integrated into a lumped-element system.

Note added.—After the paper was written, we found a preprint also studying the level-attraction effect in planar cavity, but with a different cavity design; see arXiv:1901.01729, 2019.

APPENDIX: DESIGN AND CHARACTERIZATION OF THE CAVITY

Inspired by the well-known performance of interferometric techniques, which can operate over a large frequency range and have an excellent signal-to-noise ratio in magnetic resonance experiments [47,48], we use a microstrip cross junction to fabricate a Michelson-like interferometer. The microstrip-cross-junction topology is depicted in Fig. 5(a). This cross-shaped microstrip is fabricated with use of two perpendicular 1.67-mm-wide transmission lines on a 0.813-mm-thick RO4003C substrate. The two horizontal arms are connected to a vector network analyzer to enable microwave-transmission measurements, while the two vertical arms are short-terminated, acting as the boundaries of the cavity. Each arm shares the same characteristic impedance $Z_0 = 50$ Ω and electrical length
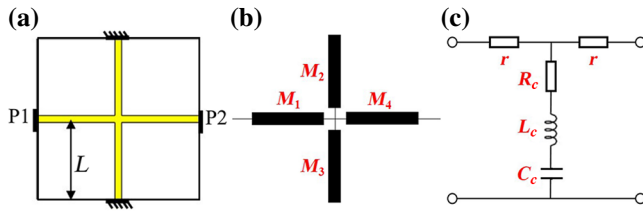
(a) **(b)** **(c)**

FIG. 5. (a) Design of a Michelson-type microwave interferometer with two short-terminated vertical arms and two horizontal arms. (b) The ideal topology of the interferometer consists of two series transmission lines and two short-ended shunt stubs with the same impedance and electrical length. The individual *ABCD* matrices are given by M_1, M_2, M_3, and M_4. (c) Equivalent circuit of the interferometer.

$\theta = kL$. $L = 20$ mm is the real length of each arm and $k = i\alpha + \beta$ is the complex wave number in a lossy material [49]. The attenuation constant is α and the phase constant $\beta = \omega/v_p$, v_p is the phase velocity in the medium.

Because the feature dimensions of the cross junction are much smaller than the wavelength of the microwaves used, the scattering properties of our device can be modeled by the cascade matrices M_1, M_2, M_3, and M_4 shown in Fig. 5(b). To compute the *ABCD* matrix for the whole cavity, we can simply multiply the matrices of the individual two-port elements [48]:

$$\begin{pmatrix} A & B \\ C & D \end{pmatrix} = M_1 M_2 M_3 M_4$$

$$= \begin{pmatrix} 2\cos 2\theta + 1 & 2jZ_0 \sin 2\theta \\ -2j\dfrac{\cos 2\theta \cot \theta}{Z_0} & 2\cos 2\theta + 1 \end{pmatrix},$$

(A1a)

where

$$M_1 = M_4 = \begin{pmatrix} \cos\theta & jZ_0 \sin\theta \\ j\dfrac{1}{Z_0}\sin\theta & \cos\theta \end{pmatrix}, \quad (A1b)$$

$$M_2 = M_3 = \begin{pmatrix} 1 & 0 \\ \dfrac{1}{jZ_0 \tan\theta} & 1 \end{pmatrix}. \quad (A1c)$$

From this *ABCD* matrix, the transmission parameter can be derived as

$$S_{21} = \frac{2}{A + B/Z_0 + CZ_0 + D} = \frac{1}{2}e^{i2\theta}(1 - e^{i2\theta}), \quad (A2a)$$

which results in a resonant dip of the transmission spectrum at $\omega = \omega_c$.

For the near-resonant condition, $\alpha L \ll 1$, so $e^{-2\alpha L} = \Gamma \approx 1$ is smaller than 1 [48]. Furthermore, $\beta_c = n\pi/L = $

ω_c/v_p when n is an integer, so $e^{i2\beta_c L} = 1$, and Eq. (A2a) can be rewritten as

$$S_{21} \approx \frac{1}{2}\left(1 - \frac{i\gamma_{ce}}{\omega - \omega_c + i(\gamma_{ce} + \gamma_{ci})}\right), \quad (A2b)$$

where $\gamma_{ce} = \Gamma(v_p/2L)$ and $\gamma_{ci} = (1-\Gamma)(v_p/2L)$ are the extrinsic and intrinsic damping of the cavity.

Figure 5(c) shows the equivalent phenomenological *LCR*-circuit model that quantitatively describes the resonant behavior. The circuit consists of lumped elements of resistance r and R_c, inductance L_c, and capacitance C_c. The matrix of this circuit is

$$\begin{pmatrix} A & B \\ C & D \end{pmatrix} = \begin{pmatrix} 1 + \dfrac{r}{Z_c} & r\left(2 + \dfrac{r}{Z_c}\right) \\ \dfrac{1}{Z_c} & 1 + \dfrac{r}{Z_c} \end{pmatrix} \quad (A3)$$

This lumped-circuit *ABCD* matrix must correspond to Eq. (A1a), which allows us to identify the two small symmetric resistances $r = jZ_0 \tan\theta \ll Z_0$, which contribute the extrinsic losses, and a shunt impedance $Z_c = R_c + j\omega L_c + (1/j\omega C_c) = jZ_0 \tan\theta/(2\cos 2\theta)$, which describes the cavity resonance. Defining $\omega_c = 1/\sqrt{L_c C_c}$, $\gamma_{ce} = (Z_0 + r)/4L_c$, and $\gamma_{ci} = R_c/2L_c$, we find that the transmission equation derived from the circuit model is the same
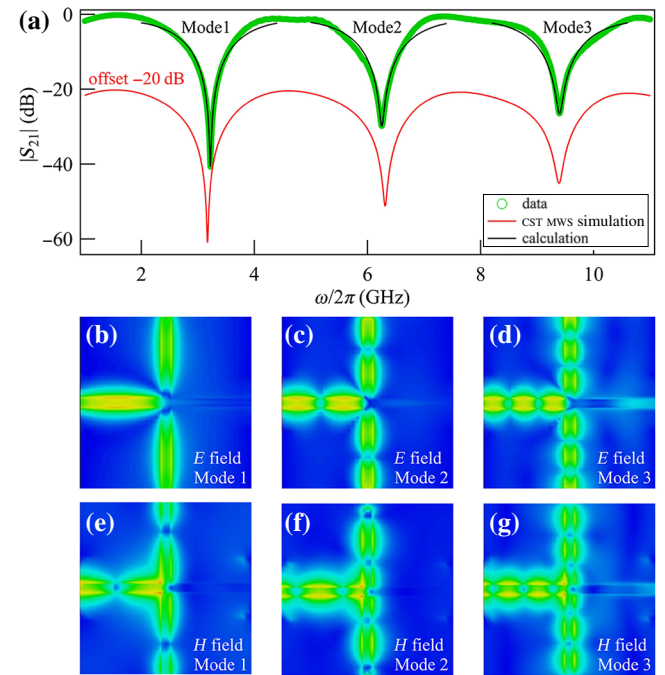
(a)

(b) **(c)** **(d)**

(e) **(f)** **(g)**

FIG. 6. (a) The cavity spectrum S_{21} is shown as green symbols, with black and red curves corresponding to the theoretical calculation and CST MWS simulations (-20 dB offset), respectively. The resulting interference fringes of the rf electric field of mode 1, mode 2, and mode 3 are shown in (b)–(d), while the rf-magnetic-field distributions are shown in (e)–(g).

TABLE I.   Resonance frequency (ω_c), extrinsic damping (γ_{ce}), and intrinsic damping (γ_{ci}) of modes 1, 2, and 3.

	Mode 1	Mode 2	Mode 3
$\omega_c/2\pi$ (GHz)	3.22	6.253	9.39
$\gamma_{ce}/2\pi$ (GHz)	0.99	0.99	0.99
$\gamma_{ci}/2\pi$ (GHz)	0.010	0.034	0.052

as Eq. (A2b). We note that $\gamma_{ci} \ll \gamma_{ce}$ since $1 - \Gamma \ll \Gamma$ and $R_c \ll \frac{1}{2}(Z_0 + r)$.

The performance of this Michelson-type microwave interferometer is first characterized with a vector-network-analyzer measurement; see the green circles in Fig. 6(a). The three resonant modes are labeled "mode 1," "mode 2," and "mode 3." Using Eq. (A2b) (black curves), we can calculate the resonant features, with the resonance frequency ω_c, extrinsic damping γ_{ce} and intrinsic damping γ_{ci} determined on the basis of a fit to the experimental data in Fig. 6(a) and summarized in Table I. As expected, all modes share the same extrinsic damping, while the intrinsic damping increases with the resonance frequency, which may be due to interference effects. The resonant features are also reproduced by CST MWS, and are plotted as the red curve with a -20-dB offset. To clearly see the interference pattern, the resulting interference fringes of the rf electric field and magnetic field, as modeled by CST MWS, are shown in Figs. 6(b)–6(g), in which color variance reflects the absolute electric or magnetic field strength. As a result, a minimum transmission (S_{21}) appears.

---

[1] G. Khitrova, H. Gibbs, F. Jahnke, M. Kira, and S. Koch, Nonlinear optics of normal-mode-coupling semiconductor microcavities, Rev. Mod. Phys. **71**, 1591 (1999).

[2] J.-M. Raimond, M. Brune, and S. Haroche, Manipulating quantum entanglement with atoms and photons in a cavity, Rev. Mod. Phys. **73**, 565 (2001).

[3] Z.-L. Xiang, S. Ashhab, J. You, and F. Nori, Hybrid quantum circuits: Superconducting circuits interacting with other quantum systems, Rev. Mod. Phys. **85**, 623 (2013).

[4] M. Aspelmeyer, T. J. Kippenberg, and F. Marquardt, Cavity optomechanics, Rev. Mod. Phys. **86**, 1391 (2014).

[5] C.-M. Hu, Dawn of cavity spintronics, Phys. Can. **72**, 76 (2016).

[6] M. Harder and C.-M. Hu, in *Solid State Physics*, edited by R. E. Camley and R. L. Stamps (Academic Press, Cambridge, 2018), Vol. 69, p. 47.

[7] S. Sharma, Y. M. Blanter, and G. E. W. Bauer, Optical Cooling of Magnons, Phys. Rev. Lett. **121**, 087205 (2018).

[8] G. Khitrova, H. Gibbs, M. Kira, S. W. Koch, and A. Scherer, Vacuum Rabi splitting in semiconductors, Nat. Phys. **2**, 81 (2006).

[9] A. Wallraff, D. I. Schuster, A. Blais, L. Frunzio, R.-S. Huang, J. Majer, S. Kumar, S. M. Girvin, and R. J. Schoelkopf, Strong coupling of a single photon to a superconducting qubit using circuit quantum electrodynamics, Nature **431**, 162 (2004).

[10] J. Majer, J. Chow, J. Gambetta, J. Koch, B. Johnson, J. Schreier, L. Frunzio, D. Schuster, A. Houck, A. Wallraff, A. Blais, M. Devoret, S. Girvin, and R. Schoelkopf, Coupling superconducting qubits via a cavity bus, Nature **449**, 443 (2007).

[11] Mika A. Sillanpää, Jae I. Park, and Raymond W. Simmonds, Coherent quantum state storage and transfer between two phase qubits via a resonant cavity, Nature **449**, 438 (2007).

[12] K. Hennessy, A. Badolato, M. Winger, D. Gerace, M. Atatüre, S. Gulde, S. Fält, E. L. Hu, and A. Imamoğlu, Quantum nature of a strongly coupled single quantum dot–cavity system, Nature **445**, 896 (2007).

[13] S. Gröblacher, K. Hammerer, M. R. Vanner, and M. Aspelmeyer, Observation of strong coupling between a micromechanical resonator and an optical cavity field, Nature **460**, 724 (2009).

[14] X. Song, M. Oksanen, J. Li, P. J. Hakonen, and M. A. Sillanpää, Graphene Optomechanics Realized at Microwave Frequencies, Phys. Rev. Lett. **113**, 027404 (2014).

[15] Ö. O. Soykal and M. Flatté, Strong Field Interactions between a Nanomagnet and a Photonic Cavity, Phys. Rev. Lett. **104**, 077202 (2010).

[16] H. Huebl, C. W. Zollitsch, J. Lotze, F. Hocke, M. Greifenstein, A. Marx, R. Gross, and S. T. Goennenwein, High Cooperativity in Coupled Microwave Resonator Ferrimagnetic Insulator Hybrids, Phys. Rev. Lett. **111**, 127003 (2013).

[17] Y. Tabuchi, S. Ishino, T. Ishikawa, R. Yamazaki, K. Usami, and Y. Nakamura, Hybridizing Ferromagnetic Magnons and Microwave Photons in the Quantum Limit, Phys. Rev. Lett. **113**, 083603 (2014).

[18] L. Bai, M. Harder, Y. Chen, X. Fan, J. Xiao, and C.-M. Hu, Spin Pumping in Electrodynamically Coupled Magnon-Photon Systems, Phys. Rev. Lett. **114**, 227201 (2015).

[19] M. Goryachev, W. G. Farr, D. L. Creedon, Y. Fan, M. Kostylev, and M. E. Tobar, High-Cooperativity Cavity QED with Magnons at Microwave Frequencies, Phys. Rev. Appl. **2**, 054002 (2014).

[20] N. Kostylev, M. Goryachev, and M. E. Tobar, Superstrong coupling of a microwave cavity to yttrium iron garnet magnons, Appl. Phys. Lett. **108**, 062402 (2016).

[21] X. Zhang, C.-L. Zou, L. Jiang, and H. X. Tang, Strongly Coupled Magnons and Cavity Microwave Photons, Phys. Rev. Lett. **113**, 156401 (2014).

[22] X. Zhang, C.-L. Zou, N. Zhu, F. Marquardt, L. Jiang, and H. X. Tang, Magnon dark modes and gradient memory, Nat. Commun. **6**, 8914 (2015).

[23] Y. Tabuchi, S. Ishino, A. Noguchi, T. Ishikawa, R. Yamazaki, K. Usami, and Y. Nakamura, Coherent coupling between a ferromagnetic magnon and a superconducting qubit, Science **349**, 405 (2015).

[24] H. Maier-Flaig, M. Harder, R. Gross, H. Huebl, and S. T. Goennenwein, Spin pumping in strongly coupled magnon-photon systems, Phys. Rev. B **94**, 054433 (2016).

[25] B. Yao, Y. S. Gui, J. W. Rao, S. Kaur, X. S. Chen, W. Lu, Y. Xiao, H. Guo, K.-P. Marzlin, and C.-M. Hu, Cooperative polariton dynamics in feedback-coupled cavities, Nat. Commun. **8**, 1437 (2017).

[26] J.-M. Pirkkalainen, S. Cho, J. Li, G. Paraoanu, P. Hakonen, and M. Sillanpää, Hybrid circuit cavity quantum electrodynamics with a micromechanical resonator, Nature **494,** 211 (2013).

[27] M. Delbecq, V. Schmitt, F. Parmentier, N. Roch, J. Viennot, G. Féve, B. Huard, C. Mora, A. Cottet, and T. Kontos, Coupling a Quantum Dot, Fermionic Leads, and a Microwave Cavity on a Chip, Phys. Rev. Lett. **107,** 256804 (2011).

[28] V. Singh, S. Bosman, B. Schneider, Y. M. Blanter, A. Castellanos-Gomez, and G. Steele, Optomechanical coupling between a multilayer graphene mechanical resonator and a superconducting microwave cavity, Nat. Nanotechnol. **9,** 820 (2014).

[29] I. Chiorescu, Y. Nakamura, C. Harmans, and J. Mooij, Coherent quantum dynamics of a superconducting flux qubit, Science **299,** 1869 (2003).

[30] A. A. Abdumalikov Jr., O. Astafiev, Y. Nakamura, Y. A. Pashkin, and J. Tsai, Vacuum Rabi splitting due to strong coupling of a flux qubit and a coplanar-waveguide resonator, Phys. Rev. B **78,** 180502 (2008).

[31] S. Kaur, B. Yao, Y.-S. Gui, and C.-M. Hu, On-chip artificial magnon-polariton device for voltage control of electromagnetically induced transparency, J. Phys. D: Appl. Phys. **49,** 475103 (2016).

[32] M. Harder, Y. Yang, B. Yao, C. Yu, J. Rao, Y. Gui, R. Stamps, and C.-M. Hu, Level Attraction due to Dissipative Magnon-Photon Coupling, Phys. Rev. Lett. **121,** 137203 (2018).

[33] N. Bernier, L. Tóth, A. Feofanov, and T. Kippenberg, Level attraction in a microwave optomechanical circuit, Phys. Rev. A **98,** 023841 (2018).

[34] J. Okolowicz, M. Ploszajczak, and I. Rotter, Dynamics of quantum systems embedded in a continuum, Phys. Rep. **374,** 271 (2003).

[35] Vahram L. Grigoryan, Ka Shen, and Ke Xia, Synchronized spin-photon coupling in a microwave cavity, Phys. Rev. B **98,** 024406 (2018).

[36] A. B. Pippard, *The Physics of Vibration* (Cambridge University Press, Cambridge, 2007).

[37] M. E. Tobar and D. G. Blair, A generalized equivalent circuit applied to a tunable sapphire loaded superconducting cavity, IEEE Trans. Microw. Theory Tech. **39,** 1582 (1991).

[38] A. Serga, A. Chumak, and B. Hillebrands, YIG magnonics, J. Phys. D: Appl. Phys. **43,** 264002 (2010).

[39] W. Barry, A broad-band, automated, stripline technique for the simultaneous measurement of complex permittivity and permeability, IEEE Trans. Microw. Theory Techn. **34,** 80 (1986).

[40] J.-S. G. Hong and M. J. Lancaster, *Microstrip Filters for RF/Microwave Applications*, Vol. 167 (John Wiley & Sons, New York, 2004).

[41] F. W. Grover, *Inductance Calculations: Working Formulas and Tables* (Courier Corporation, Mineola, 2004).

[42] A. Zangwill, *Modern Electrodynamics* (Cambridge University Press, Cambridge, 2013).

[43] W. G. Hurley and M. C. Duffy, Calculation of self and mutual impedances in planar magnetic structures, IEEE Trans. Magn. **31,** 2416 (1995).

[44] G. S. Agarwal, *Quantum Optics* (Cambridge University Press, Cambridge, 2012).

[45] M. Harder, P. Hyde, L. Bai, C. Match, and C.-M. Hu, Spin dynamical phase and antiresonance in a strongly coupled magnon-photon system, Phys. Rev. B **94,** 054403 (2016).

[46] C. Sames, H. Chibani, C. Hamsen, P. A. Altin, T. Wilk, and G. Rempe, Antiresonance Phase Shift in Strongly Coupled Cavity QED, Phys. Rev. Lett. **112,** 043601 (2014).

[47] I. S. Krishna, R. K. Barik, and S. Karthikeyan, A dual-band crossover using cross-shaped microstrip line for small and large band ratios, Int. J. Microw. Wireless Technol. **9,** 1629 (2017).

[48] E. R. Edwards, A. B. Kos, M. Weiler, and T. J. Silva, A microwave interferometer of the Michelson-type to improve the dynamic range of broadband ferromagnetic resonance measurements, IEEE Magn. Lett. **8,** 1 (2017).

[49] D. M. Pozar, *Microwave Engineering* (John Wiley & Sons, New York, 2009).